Journal of
Materials Chemistry C

Materials for optical, magnetic and electronic devices

Accepted Manuscript

This article can be cited before page numbers have been issued, to do this please use: S. C. S. Lemos, P. Serna-Gallén, L. Gracia, E. D. O. Gomes, H. Beltran-Mir, E. Cordoncillo and J. Andres, *J. Mater. Chem. C*, 2026, DOI: 10.1039/D6TC00645K.

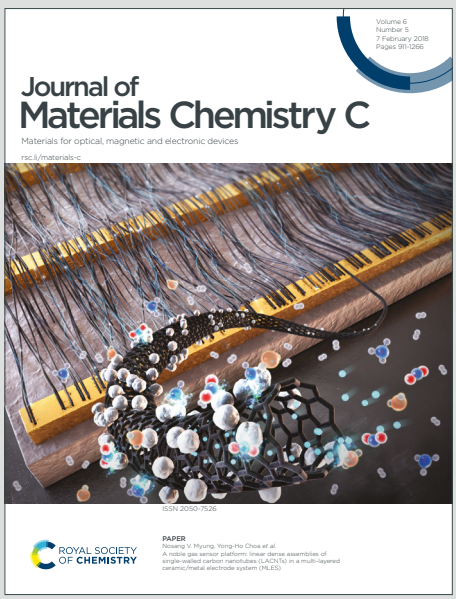

ROYAL SOCIETY OF CHEMISTRY

rsc.li/materials-c

View Article Online
DOI: 10.1039/D6TC00645K

Chemical and physical pressure meet: deciphering the polymorphism and morphology of α- and δ-KY_3F_{10} induced by Eu^{3+} doping

Samantha Custódio Silva Lemos*[1], Pablo Serna-Gallén[2], Lourdes Gracia[1,3]*, Eduardo O. Gomes[1], Héctor Beltrán-Mir[2], Eloísa Cordoncillo[2], Juan Andrés[1]*

[1]*Departament of Physical and Analytical Chemistry, Universitat Jaume I, Av. Vicent Sos Baynat s/n 12071, Castelló de la Plana, Spain*
[2]*Departament of Inorganica and Organic Chemistry, Universitat Jaume I, Av. Vicent Sos Baynat s/n 12071, Castelló de la Plana, Spain*
[3]*Department of Physical Chemistry, University of Valencia (UV), 46100 Burjassot, Spain*
*Corresponding Authors

Abstract

An atomic-level understanding of the local effects on the structure and electronic properties provoked by chemical and/or physical pressure are essential; however, their intricate relationship is poorly understood, which poses a challenge for the design of new inorganic materials with tailored properties. In this work, we report the synthesis and comprehensive characterization of pure α- and δ-KY_3F_{10} polymorphs with varying Eu^{3+}-doping levels (10-40%) revealing how the chemical (substitution of Y^{3+} by Eu^{3+})-physical pressure effects can be separated to provide fundamental insight into their stability, electronic properties, and morphology of both polymorphs. Our results consist of XRD, ICP-MS, FT-IR, and HRSEM measurements in combination with DFT calculations. Experimental and theoretical findings disclose a coupling mechanism in α- and δ-KY_3F_{10} polymorphs, despite their otherwise near-identity, in which the negative pressure effect of the δ-KY_3F_{10} polymorph is accompanied by subtle structural distortion and changes in the electronic configuration associated with the local coordination of Eu^{3+} at the [EuF_8] cluster, from C_{2v} to C_{4v} symmetry. We assess the local atomic arrangements and stability of (100), (110) and (111) surfaces of both polymorphs, the morphologies of HRSEM images, the expected pathways and corresponding barrier heights connecting them are reproduced with remarkable accuracy. This work delivers mechanistic insights into the transition between α- and δ-KY_3F_{10} polymorphs at low concentration of Eu^{3+}-doping and offers a theoretical basis to disentangle the chemical and physical pressure, providing a novel perspective for the rational design of high-performance KY_3F_{10}-based structures.

Keywords: α-,δ-KY_3F_{10} polymorphs; Chemical (Eu^{3+} doping) pressure; Physical pressure; Morphology.

View Article Online
DOI: 10.1039/D6TC00645K

I. Introduction

Crystal structures of inorganic materials can present different polymorphs with the same chemical composition, and often exhibit differing physical properties, depending on how they were synthesized or the conditions under which they operate, such as pressure, temperature, doping, and so on[1]. Polymorphism is a common phenomenon of these crystalline materials, and in recent years, the discovery not only of the stability and functionality of new phases but also their capacity to undergo phase transitions is therefore particularly important in the development of materials in diverse scientific and industrial fields[2].

Pressure, like temperature, is a fundamental thermodynamic variable that plays an important role in the induced structural transitions by tuning the lattice of inorganic material to obtain metastable polymorphs with unusual properties that are otherwise not evident under ambient conditions[3-9]. Such metastable phases have emerged as a promising class of materials thanks to their unique electronic structures, distinctive chemical bonding, specific morphologies, and ultimately for the realization of novel functions and applications[10-12]. However, the development of metastable phases still faces great challenges due to their native thermodynamic instability, calling for innovative synthetic methods and design strategies[13]. From the experimental side, high-pressure experiments, while enormously powerful, are limited not only by the high cost, usually low yields of metastable phases with larger volumes (lower density), making it hard to realize large-batch production for applications[14,15].

On the other hand, chemical pressure associated to the substitution or doping processes are the most common procedure to modify its intrinsic structure and properties of inorganic materials while changing its composition *via* lattice strain due to the different atomic radii and electronic and/or magnetic behaviors of the cations involved in the

View Article Online
DOI: 10.1039/D6TC00645K

substitution process, which is realized by a chemical method instead of a physical one, and thus has an important influence on materials properties[16-20]. In particular, the incorporation of a larger ion leads to an expansion of the crystal lattice, an effect equivalent to an effective negative external pressure, in the sense that it produces a structural dilation analogous to that generated by a decrease in the applied hydrostatic pressure. Application of both types of pressure allows not only tuning the physicochemical properties of materials by changing chemical interactions and modifying the electronic structure, but also induces phase transitions to reach new polymorphs with enhanced or novel functional properties[21-22]. In this connection, a detailed knowledge of local lattice distortions and respective effects of chemical and physical pressure when they are supplied in inorganic materials is of major importance[23-24]. However, no adequate experimental and theoretical tools have been described in the literature so far.

Chemical and physical pressure often compete or coexist along the substitution process. While it is possible to resolve both, their innate complexity means it is nontrivial to unambiguously assign one to the other. Specifically, a comprehensive picture capturing the phenomena at play and the underlying rules that govern chemistry and physics is still under development. By using density functional theory (DFT) calculations, we have previously correlate chemical pressure with physical pressure, and how the structural and electronic properties are modified by the formation of solid solutions, involving different semiconductors based on complex metal oxides, such as $NiW_{1-x}Mo_xO_4$ (x = 25, 50, and 75%)[25] and α-$Ag_{2-2x}Cu_xWO_4$ ($0 \leq x \leq 0.16$)[26]. In this scenario, we were capable of disentangle the interactions associated with the doping process, which can be differentiated from the pressure along the formation of $SnMo_{1-x}W_xO_4$ (x = 0–1) solid solution[20], and additionally, we performed polymorph-controlled synthesis of the

View Article Online
DOI: 10.1039/D6TC00645K

different polymorphs of Ag_2WO_4 [27]. On the other hand, we have developed a method to obtain the available morphologies of a given material and applied it to investigate the crystal growth mechanisms, catalytic activity, and photoluminescence emissions[28-30]. Despite remarkable findings based on experimental structural characterization techniques, there are still open questions concerning polymorphism and morphology, including but not limited to cation distribution, bonding state, structural transformation, and morphology changes in many cases, material-specific.

A particularly important class of materials is the yttrium fluorides family that possesses a plethora of stoichiometries and a wide variety of ionic metal-fluorine bonding, as can be found in crystallography databases [31-34]. This diversity facilitates the possibility of tuning their physical and chemical properties, as their study has driven development in different applications over the last few years [35-36]. Among them, recent literature has highlighted renewed interest in potassium yttrium fluoride (KY_3F_{10}) with numerous studies exploring its polymorphism to tailor its optical and electronic properties, such as magnetic resonance imaging[37], biosensors[38], theranostics[39] and high thermal sensitivity and upconversion luminescence, making them prime candidates for advanced photonic applications[40-41]. In addition, electrical and dielectric investigations of the conduction processes in KY_3F_{10} crystals have been reported[42]. KY_3F_{10} presents two polymorphs with cubic structures, although with different space groups: the α-phase belongs to the $Fm\bar{3}m$ (225), with 8 formula units per unit cell, $Z = 8$ [43], while the δ-polymorph belongs to the $Fd\bar{3}m$ (227) and has $Z = 16$. Both structures are composed of clusters of octahedrally arranged yttrium-centered square antiprisms [YF_8], which share corners and edges to generate the fluorine cubes and cuboctahedra[44].

Beyond the scope of potential applications, KY_3F_{10} also serves as an excellent model of host systems. Previously, some of us were engaged in a research project to

View Article Online
DOI: 10.1039/D6TC00645K

synthesize pure and Eu^{3+}-doped KY_3F_{10} crystal phases by different methods, and to study the intriguing physics of their optical properties[45-47]. Polymorphism of KY_3F_{10} is complex, and controlling the crystallization of α- and δ- polymorphs is a challenge. The conditions that modulate their luminescence emissions by Eu^{3+}doping have also been identified, underscoring its advantage in accessing new structure–property regimes for rare-earth yttrium fluoride phosphors[48-50]. In addition, a transition between the α/δ polymorphs has been reported for Eu^{3+}-doped KY_3F_{10} compounds using different pH values of the reaction medium[51]. These differ only through the packing arrangement of local-range symmetry, C_{4v} and C_{2v}, due to the polar distortions of eight-coordinate Eu^{3+}-centered square antiprisms [YEu_8], from becoming averaged out within α and δ crystal, respectively. The δ polymorph was kinetically trapped as a result of the synthetic conditions; however, there are still many open questions about the underlying structural mechanisms, at the atomic scale, of the stabilization process. In addition, determining polymorph stability and phase transitions remains a major challenge in crystal structure prediction. The α/δ-KY_3F_{10} polymorphs offer a unique opportunity to investigate the structural and electronic changes induced by the substitution of Y^{3+} by Eu^{3+} and physical pressure. Multiple routes to achieve phase control have been explored, such as cation exchange and pressure. While these routes have opened doors to phase manipulation, the former has limitations on which structures can be formed, and the latter does not directly target the product structure. Specifically, a comprehensive picture that captures the phenomena at play and the underlying rules that govern the α/δ-KY_3F_{10} polymorphs and the analysis of morphological changes with the substitution of Y^{3+} by Eu^{3+} is still scarce. This requires new experimental and theoretical approaches to gain insight into the effects of chemical and physical pressure, which have not been assessed and compared in full detail.

View Article Online
DOI: 10.1039/D6TC00645K

To take further steps towards clarifying the intriguing relationship between Eu^{3+} doping (chemical pressure) and physical pressure of pure and Eu^{3+} doped α-,δ-KY_3F_{10} polymorphs, this work aims to provide a sound response to this question by focusing on the structure and stability of these polymorphs, quantifying their thermodynamic accessibility and the contribution of individual lattice sites. Studying them is a highly fruitful endeavor, while at the same time challenging. Bridging this knowledge gap necessitates the synergy of experimental measurements with robust DFT calculations for rationalizing experimental results and understanding material properties. Herein, X-ray diffraction (XRD), infrared spectra (IR), and inductively coupled plasma mass spectrometry (ICP-MS) were employed for structural and elemental analysis. Then, we further investigated their morphology by high-resolution scanning electron microscopy (HRSEM). A model based on the combination of calculated surface energies and Wulff construction is proposed to explain and predict the available morphologies of both polymorphs. An attempt was then made to establish a relationship between chemical and physical pressure based on the structural and morphological characterization results.

Therefore, the main aims of the present article are threefold: first, we will find how and where chemical and physical pressure meet in the α- and δ-KY_3F_{10} polymorphs. Second, to unveil the influence of the spin configuration of the incorporated Eu^{3+} and disclose a correlation along the substitution process of Y^{3+} by Eu^{3+} between the pressure-induced phase transition, and the negative linear compressibility of the δ-KY_3F_{10} polymorph. Third, the surface stability of various crystallographic surfaces of pure and doped α- and δ-KY_3F_{10} polymorphs is assessed. Based on these findings, the map of available morphologies is constructed, which allows a close match between experimental HRSEM images and the computational thermodynamic model derived from the results of DFT calculations and Wulff construction.

View Article Online
DOI: 10.1039/D6TC00645K

II. Results and discussion

α- and δ-polymorphs can be described in terms of the minimal building block, i.e, $[YF_8]$ cluster, in which the Y^{3+} central cation displays a C_{4v} and C_{2v} local symmetry, respectively. The cluster we chose for our study serves as an appropriate model to explore the degree of structural changes in both polymorphs, which ultimately affect the stability with incorporated Eu^{3+} cations. A 3D representation of both α and δ- KY_3F_{10} structures is presented in **Figure 1**, in which the non-centrosymmetric Eu^{3+} site environment at $[YF_8]$ cluster is highlighted.

Figure 1. 3D illustration of α- KY_3F_{10} (a) and δ- KY_3F_{10} (b) structures, highlighting the local coordination of Y^{3+} cation with C_{4v} and C_{2v} symmetry, respectively. The purple, blue, and yellow spheres represent the K, F, and Y atoms.

Before the detailed analysis of differences between experimental data and model predictions, it is crucial to note here the assumptions made in our theoretical approach. First, taking into account hybrid functionals such as PBE0 to mitigate the self-interaction error present in GGA functionals and providing improved band-gap estimates[52-53]**.** Second, to enhance the accuracy of understanding and predicting in the high-spin structures within the PBE0 functional, yet its theoretical description poses a challenge for common excited state methods. Despite facing challenges due to existing technical and theoretical constraints and given the typical uncertainties in experimentally measured atomic distances (±0.01 Å), a good agreement among measurements, previous reports, and calculated geometry (lattice parameters, bond distances, and angles) by using this functional is found (see **Table 1**). It is important to note the significant volume expansion of ca. 7.8% of δ–KY_3F_{10} polymorph with respect to α, associated with enlarged crystallographic repeat units (higher Z, from 8 to 16). In the calculated α–phase, the $[YF_8]$

View Article Online
DOI: 10.1039/D6TC00645K

square antiprism cluster is distorted, and hence, has four Y-F bond distances of 2.21 Å and four Y-F bond distances of 2.36 Å. The δ-phase presents a more distorted local environment for Y^{3+} cations; the [YF_8] square antiprism cluster has four Y-F bond distances of 2.24 Å, two with 2.31 Å and two with 2.36 Å, consistent with previous experimental results[54]. An analysis of the DFT-optimized structures points out a [YF_8] square antiprism flattening from α to δ- polymorph, leading to reduced symmetry, from C_{4v} to C_{2v}, respectively. Consequently, the material may exhibit local structural reorganization rather than a complete phase transition (with an energy difference between the two polymorphs of 0.306 eV), involving a shift from a distorted cubic structure $Fm\bar{3}m$ to a more asymmetric $Fd\bar{3}m$.

Table 1. Experimental and calculated values of the geometry (cell parameters, bond lengths, and bond angles), band gap, and total energy of α– and the δ–KY_3F_{10} polymorphs.

The rare-earth cations, Y^{3+} and Eu^{3+}, share many comparable chemical and physical properties due to their similar oxidation states, electronegativity, ionic radius (1.019 Å for Y^{3+} and 1.066 Å for Eu^{3+} with a coordination number = 8)[55]. In addition, the electron configuration in the outer valence shell is Y^{3+}-[Kr] while Eu^{3+} has additional 4*f* orbitals that fill up after the [Xe] shell, i.e., Eu^{3+}-[Xe] $4f^6$. Hence, their introduction does not create oxygen vacancies in the structure because charge balancing is maintained. The nominal percentages of Eu^{3+} used were: 10, 15, 20, 30, 40, 50, and 100 mol% with respect to the total amount of Ln (Ln = Y, Eu). Samples were denoted as "S-*n*", where *n* indicates the percentage of Eu^{3+}. The XRD analysis of Eu^{3+}-doped samples (up to 40 mol% Eu^{3+}) provides insight into their structural characteristics. As shown in **Figure 2**, in which the XRD cards of cubic δ-$KY_3F_{10}{\cdot}xH_2O$ (ICSD card 04-016-7073), cubic α-KY_3F_{10} (ICSD card 00-040-9643), and orthorhombic YF_3 (ICDD card 00-032-1431) have been included

View Article Online
DOI: 10.1039/D6TC00645K

to serve as references, the sharp and intense peaks suggest high crystallinity with well-defined lattice planes. XRD patterns of sample S-10 (10 mol% Eu^{3+}) unequivocally demonstrate the phase purity of the synthesized sample, with solely exhibiting the characteristic of δ-phase, with no traces or impurities of other crystal structures. Low-intense peaks corresponding to the α-phase appear in the XRD pattern of sample S-15 (15 mol% Eu^{3+}), being more prominent as the Eu^{3+} content increases. Indeed, the presence of both α- and δ-phases is very clear in sample S-30 (30 mol% Eu^{3+}). The same peaks are present without additional peaks corresponding to europium oxides. The absence of secondary phases suggests that Y^{3+} cations are successfully substituted by Eu^{3+} within the lattice, rather than forming separate europium oxide compounds; however, higher percentages of the Eu^{3+} induce the presence of secondary phases, which can be ascribed to YF_3 (see sample S-40), being more evident at higher percentages of Eu^{3+} (samples S-50 and S-100), as it is presented in the Supporting Information. The incorporation of Eu^{3+} into the KY_3F_{10} matrix induces lattice strain, evident from the slight broadening of diffraction peaks.

Figure S1 of the SI shows the XRD patterns of samples S-50 and S-100, mainly composed of YF_3, hexagonal EuF_3, and orthorhombic EuF_3 phases.

Figure 2. XRD patterns of samples doped with Eu^{3+} in the range 10–40 mol%. The peaks indicated with red triangles are associated with the α-phase, while those highlighted with green diamonds refer to the presence of orthorhombic YF_3.

The IR spectra of the prepared samples are presented in **Figure 3**. In the low-energy region, 200-600 cm^{-1} (**Figure 3b**), prominent bands are observed for S30 and S40 samples at 231, 276, and 364 and 500 cm^{-1}, assigned to α-KY_3F_{10} structure, while the bands at 215, 241, and 295 and 395 cm^{-1} for S10, S15, and S20 samples correspond to δ-KY_3F_{10} structure. Calculated IR spectra for pure (black) and doped (colored) α and δ

View Article Online
DOI: 10.1039/D6TC00645K

phases can be seen in **Figure 3c**. The IR frequencies of the prepared samples (S10 and S20), as well as the calculated IR frequencies of α and δ-KY_3F_{10} polymorphs at 16.7% and 8.3% of Eu^{3+} doping, are presented in **Table S2** of the SI. The α-KY_3F_{10} structure exhibits 8 IR-active ($8T_{1u}$) modes according to group theory analysis. The calculated IR spectra of α-KY_3F_{10} depict, as principal contributions, bands at 243, 315, and 360 cm^{-1} assigned to Y-F-K, F-Y-K, and F-Y-F bending modes, respectively, and a band at 508 cm^{-1} associated with the F-Y stretching mode. The δ-KY_3F_{10} structure exhibits 14 IR-active ($14T_{1u}$) modes according to group theory analysis. In the calculated spectra of δ-KY_3F_{10} bands attributed to bending of F-Y-F, F-Y-K, F-Y-F, and F-Y-K were observed at 228, 255, 288, and 324 cm^{-1}, respectively, and a F-Y stretching mode was observed at 414 cm^{-1}. When Y^{3+} is substituted by Eu^{3+}, new vibrational modes appear due to a symmetry-breaking process. The overlap of peaks (leads to band broadening and shifts towards lower frequencies due to subtle structural changes resulting from the Eu^{3+} doping.

Figure 3. Experimental IR spectra of samples (a), amplified region of the spectra in the range 200-600 cm^{-1} (b), and calculated IR spectra for the α and δ crystal phases, pure (black) and doped (colored) (c). The dashed lines in (b) serve as guidelines to observe the change in the position and presence of some peaks of interest.

Next, we carry out an extensive structural optimization of Eu^{3+}-doped α and δ crystalline KY_3F_{10} polymorphs at different spin multiplicities of 5 and 7, which are denoted as M=5 and M=7, respectively. Calculated values of the geometry, band gap, and total energy of α- and δ-KY_3F_{10} polymorphs at 8.3% and 16.7 % of Eu^{3+} doping are presented in **Table 2** and **Table 3**, respectively. The substitution process is associated with a comparable energetic cost in both structures, with a very small difference of approximately (≈ 0.004 eV), suggesting that the Eu^{3+} incorporation does not strongly favor one phase over the other from a purely energetic standpoint. Therefore, the concept

View Article Online
DOI: 10.1039/D6TC00645K

of chemical pressure can be interpreted as arising primarily from local structural distortions induced by the size and electronic differences between Eu^{3+} and Y^{3+}, rather than from a large energetic driving force for substitution. The variation of bond distances around the substituted Y^{3+} by Eu^{3+} implies subtle distortions in the local environment at the [EuF_8] cluster in both α and δ polymorphs (Eu-F distances ranged in 2.26-2.40 Å and 2.28-2.39 Å, respectively). Considering this induction of a local strain and a cluster expansion, a possible phase transition to a phase with expanded volume would be expected (an effect equivalent to an effective negative external pressure).

Table 2. Calculated values of the geometry (cell parameters and bond lengths), band gap, and total energy of α- and δ-KY_3F_{10} polymorphs at 8.3% of Eu^{3+} doping at spin multiplicity M=7, and M=5 and 7, respectively.

Table 3. Calculated values of the geometry cell parameters and bond lengths), band gap, and total energy of α- and δ-KY_3F_{10} polymorphs at 16.7% of Eu^{3+} doping at spin multiplicity M=7.

The energy-volume curves for the different polymorphs are presented in **Figure 4a**, where arrows from bottom to top herein indicate phases connected across these transitions. For KY_3F_{10}, negative pressure enhances the distortion of the [YF_8] square antiprism cluster and induces a less symmetrical environment for Y^{3+} cations in passing from α to δ phase. Therefore, from the structural point of view, substituting Y^{3+} by Eu^{3+} cations (chemical pressure) provides an efficient way to expand crystalline structures. As compressions are commonly related to positive pressures and pressure and temperature opposite effects, it is interesting to use the concept of chemical pressure to offer a unified view of the entire phenomenon[7]. In an attempt to link the experimental observation of a symmetry reduction, i.e., the structural motif of the square antiprism with C_{4v} symmetry, to the square antiprism with C_{2v} symmetry. In comparison, the C_{2v} local coordination is

View Article Online
DOI: 10.1039/D6TC00645K

preferred at 8.3% Eu^{3+}, according to our calculations and in agreement with the experimentally observed overall substitution. We estimate the enthalpy variation as a function of physical pressure, presented in **Figure 4b**. This thermodynamic analysis provides a deep understanding of crystalline metastability and can be a foundation on which future kinetic theories, involving transformation barriers and metastable lifetimes, can be constructed. An analysis of the results indicates a α (*Fm3m*) to δ (*Fd3m*) phase transition at a negative pressure value of -1.2 GPa, indicating that for this transition, the volume of the involved structures is expanded. In addition, other possible phase transitions have been explored, starting from α phase: when a positive pressure is applied, a phase transition to a tetragonal structure (*P42/mmc*) [56] takes place at 15 GPa, and a phase transition α to rhombohedral structure (*R3m*), material ID *mp-34042,* is observed at high negative pressure, indicating that high temperature is needed for this transformation. The mechanism of this phase transition can be classified as a pressure-induced collapse caused by reorientation and a shift toward tighter space-filling. In addition, the phase transition from α to δ phase at -1.2 GPa, is maintained at 8.3% and 16.7% of Eu^{3+}doping (see **Figure S2** of the SI).

Figure 4. Energy-volume curves for the different studied polymorphs (a). Enthalpy variation as a function of pressure (b).

In accordance with Hund's rule of maximum multiplicity, Eu^{3+} presents a high spin such that the potential energy required to maintain a high spin configuration surpasses the spin pairing energy [57-58]. In our case, α and δ Eu^{3+}-doped KY_3F_{10} structures are dominated by ionic interactions (close-shell F^- and Eu^{3+}), which are in the meV order. The corresponding global minimum of α and δ polymorphs is located at the same high spin multiplicity. Moreover, in comparison to the 5d orbital, the 4f orbitals of Eu^{3+} possess

View Article Online
DOI: 10.1039/D6TC00645K

no significant overlap with F^- orbitals. As a consequence, the 4f electrons scarcely delocalize onto the F^- orbitals, and these interactions are not capable of breaking the degeneracy of the Eu^{3+} cation-4f orbitals at the $[EuF_8]$ cluster of α/δ-KY_3F_{10} polymorphs.

An extensive exploration of the stable configurations at different spin multiplicities is performed for both polymorphs. For the α–KY_3F_{10} polymorph at 8.3% and 16.7% Eu^{3+}, only a minimum with spin multiplicity of 7 (6 unpaired electrons at the 4f orbitals) is found (see Tables 2 and 3). The δ–KY_3F_{10} polymorph at doped 8.3%-Eu^{3+} presents two minima, at high-spin 7 (6 unpaired electrons at the 4f orbitals) and moderate-spin 5 (4 unpaired electrons). The relative stability between the α and δ–KY_3F_{10} polymorphs at 8.3% and 16.7% Eu^{3+} for the most stable structures with M=7 are 0.30 and 0.19 eV, respectively. This observation indicates the possibility for the simultaneous formation of both pure and doped polymorphs, as it appears in S-15, S-20, and S-30 (see Figure 2), or the energy required for phase transition can be achieved at relatively lower temperatures. In addition, the δ-KY_3F_{10} polymorph presents an energy between the M=7 and M=5 of 0.63 eV. Different configurations involving two Eu^{3+} substitutions at different relative positions (16.7%) were systematically examined, showing total energy differences negligible (see **Table S3** and its discussion in SI).

To gain insight into the electronic properties of pure and Eu^{3+}-doped α and δ–KY_3F_{10} polymorphs, we analyze the corresponding changes in the density of states (DOS) projected on atoms and orbitals. **Figure S3 (a)** of SI shows that both polymorphs present a wide band gap material, with the valence band (VB) being predominantly composed of F 2p orbitals, while the conduction band (CB) is from Y 4d orbitals, with a band gap for δ-and α-polymorphs of 11.2 and 11.0 eV, respectively. Projected DOS on orbitals of K^+, F^-, Y^{3+} and Eu^{3+} ions for α-phase at 8.3% Eu (M=7), α-phase at 16.7% Eu (M=7), δ–phase at 8% Eu (M=5), δ–phase at 8.3% Eu (M=7) and δ–phase at 16.7% Eu

View Article Online
DOI: 10.1039/D6TC00645K

(M=7) are depicted in **Figure S3 (b-f)**, respectively. The resulting modifications in the DOS and band gap offer a qualitative understanding of the conductivity variations observed upon Eu^{3+} doping, as these directly influence carrier availability and transport properties. For the Eu^{3+}-doped systems (where spin-up and spin-down electrons are denoted with α and β, respectively) it is observed that the presence of localized intermediate states, at the band gap, formed by empty Eu 4f orbitals, substantially modifies the DOS, enhancing the optical absorption in the visible region and electronic conductivity of both polymorphs. In general, the values of band gap decrease to 4.2 eV at 8.3% Eu^{3+} (M=7) and up to 5.5 eV at 16.7% Eu^{3+} (for M=7) for the α-phase. For the δ-phase, the gap is reduced to 4.8 eV at 8.3% Eu^{3+} for M=5, to 4.9 eV for M=7, and to 4.8 eV at 16.7% Eu^{3+}.

Figure 5 illustrates the projected DOS on the f orbitals of Eu^{3+} and their contribution in the VB region. An analysis of **Figure 5a** and **5b** shows that the VB at 8.3% Eu^{3+} are mainly contributed by half-filled f_{yz^2} orbital (40%) while at 16.7% Eu^{3+} are composed by the combination (60%) of half-filled f_{xyz} and $f_{y(3x^2-z^2)}$ orbitals. Its percentage of contribution by calculating the area below the curve corresponding to the 4f orbitals in VB of the DOS. An analysis of **Figure 5c** and **5d** of the δ-polymorph renders that the VB at 8.3% with high spin (M=7) are mainly composed by half-filled $f_{y(x^2-z^2)}$ (35%) and in a minor extent by half-filled f_{xyz} (30%), while at 16.7% Eu^{3+} by half-filled f_{xyz} (50%). At 8.3% Eu^{3+} with moderate spin (M=5) the VB is mainly composed by the filled f_{xyz} orbital (45%), while half-filled f_{xz^2} (15%) and each f_{yz^2} ,$f_{y(x^2-z^2)}$, $f_{y(3x^2-y^2)}$ orbitals contributed to 10%, as it is depicted in **Figure 5e**. These results are schematically presented in **Figure S4** of SI, in which the electron configuration for 4f orbitals are depicted for the C_{4v} and C_{2v} symmetry of $[EuF_8]$ site. The C_{4v} symmetry at 8.3% Eu^{3+} and 16.7% Eu^{3+} presents an electronic configuration with major contribution of half-filled f_{yz^2}

View Article Online
DOI: 10.1039/D6TC00645K

and f_{xyz}, $f_{y(3x^2-z^2)}$ orbitals, respectively. For 4f orbitals at the C_{2v} symmetry of the δ phase, the f orbital contribution to the VB depends not only on the Eu^{3+} doping concentration but also on the multiplicity. The C_{2v} symmetry at 8.3% and 16.7% Eu^{3+} with M=7 has an electronic configuration with major contribution of half-filled $f_{y(x^2-z^2)}$ and f_{xyz} orbitals, respectively, while at 8.3% Eu^{3+} with M=5 the most contributed orbital is the filled f_{xyz}. Moreover, Eu^{3+} doping process alters the electronic structure and band alignment of the α and δ phases of KY_3F_{10}, thereby causing a transition in the configuration and occupancy of the f orbitals of Eu^{3+} at the C_{4v} and C_{2v} symmetry of $[EuF_8]$ cluster in α and δ-polymorphs. Finally, it is interesting to note that the empty Eu 4f orbitals constitute localized intermediate states at the band gap, follow similar contributions and can be well correlated to the composition of occupied Eu 4f orbitals of VB.

Figure 5. Projected DOS on f orbitals of Eu^{3+} for α-phase, a) 8.3% Eu (M=7) and b) 16.7% Eu (M=7); for δ–phase, c) 8.3% Eu (M=5), d) 8.3% Eu (M=7), and e) 16.7% Eu (M=7). A vertical dashed line indicates the Fermi level. Spin-up and spin-down electrons are denoted with α and β

The morphologies of as-prepared samples, S-10, S-15, S-20, S-30, and S-40, obtained by using HRSEM, are presented in **Figure 6.** An analysis of the results presented herein indicates that the nanoparticles have homogeneous distribution, good dispersion**,** and small differences in the average upon the Eu^{3+}doping process. However, diverse morphologies are found, which are driven by the variation of Eu^{3+} content, from spherical in S-10 to octahedral at S-15, with a dominant (111) surface. In S-20, a cubic morphology is observed, which is composed mainly of (100) surface, while a truncated octahedra morphology is found at the S-30 sample, in which the (111) and (110) surfaces

View Article Online
DOI: 10.1039/D6TC00645K

are predominant. Lastly, in S-40, a complete set of morphologies (octahedra, truncated octahedra, and cubic) can be observed.

Figure 6. HRSEM images of (a) S-10, (b) S-15, (c) S-20, (d) S-30, and (e) S-40 samples. Well-defined morphologies have been pointed out in each image, and the corresponding models of octahedron, truncated octahedron, and a cube are highlighted for comparison purposes.

To accurately evaluate the formation energies of different crystal surfaces, the typical slab model was used in the calculations. This model is constructed by selectively exposing the plane of interest and removing a portion of the atoms to form a *vacuum*. All slab models are constrained to the symmetrical top and bottom surfaces. The values of E_{surf} can be calculated by the equation (1):

$$E_{surf} = \frac{[E_{slab} - n \cdot E_{bulk}]}{2A} \quad (1)$$

where the E_{slab} and the E_{bulk} are the total energies of the surface slab model and the bulk (unit cell), respectively; *n* refers to the number of bulk units in the slab, and *A* is the surface area for symmetric slabs. The slab surface models are stoichiometric and the convergence of the calculated surface energies with the number of layers in the slab model has been performed. The broken bonds density (D_B) of the surface was calculated by using equation (2), in which n_{BB} is the number of broken bonds in the termination, and *A* is the surface area

$$D_B = \frac{n_{BB}}{A} \quad (2)$$

The polyhedron energy, E_{pol}, is calculated using equation (3):

$$E_{pol} = \sum C_i \times E_{surf} \quad (3)$$

where C_i is the percentage of contribution of the surface area to the total area of the polyhedron, $C_i = A^i/A^{pol}$ [59].

View Article Online
DOI: 10.1039/D6TC00645K

(100), (110) and (111) surface models for the α- and δ-KY_3F_{10} are presented in **Figure 7**. An analysis of Y and K superficial clusters shows [YF_7] undercoordinated clusters for (100) surface, [YF_5] clusters for (110), and [YF_6] clusters for (111) surfaces of α-KY_3F_{10} polymorph. In addition, (110) and (111) surfaces also contain undercoordinated [KF_3] clusters. The fluorine broken bonds can be interpreted as fluorine vacancies and are written using the Kröger-Vink notation[60]. Instead, for the δ-KY_3F_{10} polymorph, undercoordinated [YF_4] and [YF_6] clusters compose the (100) surface, while the (110) and the (111) surfaces only present [YF_5] clusters. In addition, the (110) surface also contains undercoordinated [KF_5] clusters. All the studied surfaces are non-polar except the surface (e), which produces a non-zero dipole moment perpendicular to the surface with high E_{surf} value. Therefore, the (100) has the lower surface energy (E_{surf}) in α and δ polymorphs, which contain a low amount of undercoordinated Y and completely coordinated F sites. However, E_{surf} values are much higher for δ phase, due to a higher dangling bond value (D_B = 6.61 nm^{-2}) than in α polymorph (D_B = 3.34 nm^{-2}), as can be seen in **Table 4**.

Figure 7. Surface models for the α-KY_3F_{10}, a) (100), b) (110), c) (111), and for the δ-KY_3F_{10}, d) (100), e) (110), f) (111). The Y and K superficial clusters on the surfaces are shown.

Table 4. Data on thickness, area, and undercoordinated clusters, E_{surf} and D_B values for the studied surfaces of α and δ polymorphs.

Previously, we presented a framework that reveals how changing the values of E_{surf} opens a door to predicting and designing the complete map of available morphologies for a wide range of metals and metal oxides[61]. This procedure allows us to bridge a direct link between electron microscopy images and theoretical morphologies, which is applied here to complement and rationalize the experimental HRSEM images by combining E_{surf}

View Article Online
DOI: 10.1039/D6TC00645K

values of exposed (100), (110), and (111) surfaces obtained by DFT calculations and Wulff construction. A map of available morphologies for both polymorphs is presented in **Figure 8**, ordered by means of the polyhedron energy (E_{pol}) values. For α the phase, an octahedral morphology was obtained as the most stable (0.23 J/m^2), resulting from the preferential stabilization of the (111) surface. Additional morphologies can be obtained by strategically modifying the E_{surf} values of specific surfaces and considering the contribution of each surface area, achieving truncated octahedral or cubic morphologies only with a lower increase in E_{pol} values. In contrast, for δ phase (**Figure 8b**), both the octahedral and the cubic morphologies present the low values of E_{pol} (1.60 J/m^2), although with E_{pol} values higher than in α phase. The cubic morphology results from the preferential stabilization of the (100) surface, and three additional morphologies can be obtained with an increase in E_{pol} values up to 2.0 J/m^2.

Figure 8. Map of available morphologies for (a) α-KY_3F_{10} and (b) δ-KY_3F_{10} polymorphs ordered by means of E_{pol} values.

Despite the distinct morphological differences, both polymorphs exhibited essentially cubic space groups This indicates that the variation in crystal morphology arises primarily from differences in crystal growth rates rather than from changes in the underlying lattice structure. Our analysis further reveals the pathways connecting experimental/theoretical morphologies, allowing us to make a direct link between variations of the values of E_{surf} and morphology. **Figure 9** (a) and (b) show the energy profiles connecting the morphologies obtained by HRSEM images and DFT calculations of α and δ-KY_3F_{10} polymorphs, respectively, which can be correlated to the Eu^{3+} content. Confirmed by DFT calculations, the cubic and octahedral are the most stable

View Article Online
DOI: 10.1039/D6TC00645K

morphologies in δ-phase and with lower values in the α phase (0.43 and 0.23 eV, respectively), suggesting the coexistence of both morphologies, as observed in the HRSEM image of S-20. In S-30 (and S-15), only octahedral and truncated octahedral morphologies coexist, having the latter E_{pol} values of 2.0 eV and 0.35 eV for the α phases, respectively. Besides, the three morphologies (octahedral, cubic, and truncated octahedral) coexist in S-40, which can be connected from the cubic to the octahedral morphologies passing through the truncated octahedral without or with a barrier of 0.4 eV for α (Figure 8a) or δ (Figure 8b) phases, respectively. This consistency validates the picture from our model, where the values of calculated E_{surf} of the exposed surfaces and E_{pol} are involved in each pathway. These findings underscore the importance of surface effects provoked by Eu^{3+}-doping, and fit with experimental data reported for α- and δ-KY_3F_{10} polymorphs. Therefore, controlled surface synthesis is not only a rational route to study the relationship between the morphology and the surface structure dependent properties but also a feasible approach for developing highly active materials to better customize their luminescent and photocatalytic functionality. In this sense, it is expected that the δ phase, with highly active surfaces exposed in its morphology (E_{pol} values much higher than for α phase), shows superior optical and photocatalytic performance.

Figure 9. Energy profiles connecting the morphologies obtained by HRSEM images and DFT calculations of (a) α-KY_3F_{10} and (b) δ- KY_3F_{10} polymorphs.

Understanding evolution guides the design of polymorphs of inorganic semiconductors by analyzing the effect of chemical/physical pressure, revealing structure-activity relationships that provide a theoretical basis for developing new materials. It can be argued that every technological breakthrough in this field stems from a profound understanding of its mechanism. The innovation of the current work is based

View Article Online
DOI: 10.1039/D6TC00645K

on a comprehensive investigation of the polymorphism and morphology of α- and δ-KY_3F_{10} polymorphs. induced by Eu^{3+} doping (10-40%) and external pressure. It is important to note that there is a clear difference between chemical and physical pressure: the Eu^{3+} doping process regulates the α-to-δ phase transition by a subtle modification of the local electronic structure of the [EuF_8] cluster at low values of Eu^{3+} doping, while this transition is achieved under negative pressure. The fundamental reasons behind this intriguing behavior were further rationalized by in-depth integration of theoretical simulation (DFT calculations) and experimental verification (XRD, ICP-MS, FT-IR, HRSEM) techniques, which is another important trend.

III. Conclusions

The main conclusions of this work can be summarized as follows: (i) the integration of experiments results combined with DFT calculations provides an atomistic-level insights into the substitution process of Y^{3+} by Eu^{3+} and under physical pressure to unravel the interplay among structural complexity, phase metastability, and morphology change, (ii) the structural or electronic origin of the intricate relationship between chemical and physical pressure were successfully explained by subtle distortions in the local environment of Eu^{3+} at [EuF_8] cluster in both α and δ polymorphs, (iii) based on DFT results, we reveal for the first time that small differences in the local arrangements of Eu^{3+} at [EuF_8] cluster in both polymorphs follow quantum mechanical rules, which are conceptually connected to a model of energies and electronic configurations of 4f orbitals of Eu^{3+} at the coordination environment, (iv) the mechanism of α to δ phase transition can be classified as a pressure-induced collapse caused by a symmetry reduction from C_{4v} the C_{2v} of [EuF_8] cluster, (v) we estimate the enthalpy variation as a function of physical pressure and the phase transition from α to δ phase at -1.2 GPa is maintained at

View Article Online
DOI: 10.1039/D6TC00645K

8.3% and 16.7% of Eu^{3+} doping, (vi) an extensive exploration of the stable configurations at different spin multiplicities for both polymorphs was performed at 8.3% and 16.7% Eu^{3+}, and the DOS analysis reveals localized intermediate states contributed by Eu 4f orbitals which significantly narrow the effective band gap of both polymorphs, which could enhance optical absorption in the visible region, (vii) a correlation between the relative stability of Eu^{3+} doped α- and d- KY_3F_{10} polymorphs and 4f orbital occupancy at the $[EuF_8]$ cluster with C_{4v} the C_{2v} symmetry, respectively, is delineated, as a result of the meticulous manipulations of both chemical and physical pressure at the atomic level, (viii) by employing the values of surface and polyhedron energy of the DFT calculations and Wulff construction a more comprehensive picture of the changes of morphology can be performed, where these calculations were sufficient for an adequate description of different pathways connecting the spherical, octahedral, cubic and truncated octahedra of the observed morphologies.

Taken together, the novelty of the present findings lies in the disentanglement of a coupling mechanism among chemical and pressure effects, and the local structure of $[EuF_8]$ cluster, providing an understanding of the structural and electronic properties of α- δ-KY_3F_{10} polymorphs, as host materials, through controlled substitution of Y^{3+} by Eu^{3+}. The importance of the trap δ metastable phase in a KY_3F_{10} matrix is highlighted to tune the physical properties and soften the synthesis conditions in a cost-effective way. By bridging atomic-scale simulations with experimental observables, the comprehensive discussion aims to provide theoretical guidance for developing α- and δ-KY_3F_{10} polymorphs, which might be relevant for a precise polymorphic transition with tunable response characteristics.

View Article Online
DOI: 10.1039/D6TC00645K

Acknowledgments

S.C.S.L., M. J. A., and L. G. thank Universitat Jaume I (project UJI-B2022-56), Ministerio de Ciencia, Innovación y Universidades (project PID2022-141089NB-I00), and Generalitat Valenciana (CIAICO/2024/94) for financially supporting this research. S.C.S.L has been funded by Generalitat Valenciana (CIAPOS/2022/148), and E.O.G has been funded by Generalitat Valenciana (CIAPOS/2022/162). H.B.M. and E.C. thank Ministerio de Ciencia, Innovación y Universidades (Project PID2024-158224NB-I00 funded by MICIU/AEI/10.13039/501100011033 and by ERDF/EU) and Universitat Jaume I (project GACUJIMA/2025/10).

References

1. B. K. Saha, N. K. Nath, R. Thakuria, *Chem. Rec.* 2023, **23**, e202200173.

2. D. Gentili, M. Gazzano, M. Melucci, D. Jones, M. Cavallini, *Chem. Soc. Rev.* 2019, **48**, 2502–2517.

3. P. F. McMillan, *Chem. Soc. Rev.* 2006, **35**, 855–857.

4. A. Katrusiak, *Acta Crystallogr. Sect. B Struct. Sci. Cryst. Eng. Mater.* 2019, **75**, 918–926.

5. K. P. Hilleke, T. Bi, E. Zurek, *Appl. Phys. A*, 2022, **128**, 441.

6. M. Miao, Y. Sun, E. Zurek, H. Lin, *Nat. Rev. Chem.* 2020, **4**, 508–527.

7. B. C. Barnes, J. K. Brennan, E. F. C. Byrd, S. Izvekov, J. P. Larentzos, and B. M. Rice, 2019, **28**. Springer (Ed. N. Goldman)

8. E. Zurek, W. Grochala, *Phys. Chem. Chem. Phys.* 2015, **17**, 2917–2934.

9. F. Zeller, C. Hsieh, W. Dononelli, T. Neudecker, *WIREs Comput. Mol. Sci.* 2024,

View Article Online
DOI: 10.1039/D6TC00645K

14, e1708.

10. A. Parija, G. R. Waetzig, J. L. Andrews, S. Banerjee, *J. Phys. Chem. C,* 2018, **122**, 25709–25728.

11. P. A. Maggard, *Acc. Chem. Res.* 2021, **54**, 3160–3171.

12. M. Biswas, H. Nishinaka, *APL Mater.* 2022, **10**, 060701.

13. M. Aykol, S. S. Dwaraknath, W. Sun, K. A. Persson, *Sci. Adv.* 2025, **4**, eaaq0148.

14. D. Zhao, M. Wang, G. Xiao, B. Zou, *J. Phys. Chem. Lett.* 2020, **11**, 7297–7306.

15. D. D. Le Pevelen, G. E. Tranter, *Encyclopedia of spectroscopy and spectrometry*, Oxford: Academic Press, 2017, 750-761.

16. K. Lin, Q. Li, R. Yu, J. Chen, J. P. Attfield, X. Xing, *Chem. Soc. Rev.* **51**, 2022, 5351–5364.

17. H. H. Osman, M. A. Salvadó, P. Pertierra, J. Engelkemier, D. C. Fredrickson, J. M. Recio, *J. Chem. Theory Comput.* 2018, **14**, 104–114.

18. A. Lobato, H. H. Osman, M. A. Salvado, P. Pertierra, A. Vegas, V. G. Baonza, J. M. Recio, *Inorg. Chem.* **59**, 2020, 5281–5291.

19. J. M. Recio, A. Lobato, H. H. Osman, M. A. Salvadó, A. Vegas, *in Comprehensive Inorganic Chemistry III* (Elsevier), 2023, **1**, 238-261.

20. E. O. Gomes, A. F. Gouveia, L. Gracia, A. Lobato, J. M. Recio, J. Andres, *J. Phys. Chem. Lett.* 2022, **13**, 9883–9888.

21. H. L. Huang, C. Chae, J. M. Johnson, A. Senckowski, S. Sharma, U. Singisetti, J. Hwang, *APL Mater.* 2023, **11**, no. 6, 061113.

View Article Online
DOI: 10.1039/D6TC00645K

22. M. Govindhan, K. Sukumar, *J. Power Sources* **658**, 2025, 238287.

23. H. H. Osman, A. Otero-De-la-Roza, P. Rodriguez-Hernández, A. Munoz, F. J. Manjon, *J. Mater. Chem. C* **12**, 2024, 10447–10474.

24. H. H. Osman, P. Rodríguez-Hernández, A. Muñoz, F. J. Manjón, *J. Mater. Chem. C* **13**, 2025, 3774–3803.

25. A. F. Gouveia, M. Assis, L. K. Ribeiro, E. O. Gomes, M. D. Teodoro, E. Longo, J. Andres, *J. Mater. Chem. C,* 2025, **13**, 6788–6798.

26. P. F. Pereira, C. C. De Foggi, A. F. Gouveia, I. M. Pinatti, L. A. Cabral, E. Guillamon, J. Andrés, *International Journal of Molecular Sciences*, 2022, **23**, 10589.

27. R. Alvarez-Roca, A. F. Gouveia, C. C. De Foggi, P. S. Lemos, L. Gracia, L. F. Da Silva, J. Andres, *Inorg. Chem.* 2021, **60**, 1062–1079.

28. J. Andrés, L. Gracia, A. F. Gouveia, M. M. Ferrer, E. Longo *Nanotechnology*, 2015, **26**, 405703.

29. M. M. Ferrer, A. F. Gouveia, L. Gracia, E. Longo, J. Andrés, *Model. Simul. Mater. Sci. Eng.* 2016, **24**, 25007.

30. A. F. Gouveia, L. Gracia, E. Longo, M. A. San-Miguel, J. Andrés, J., *Comput. Mater. Sci.* 2021, **188**, 110217

31. Z. Mazej, E. Goreshnik, *Inorg. Chem.* 2022, **61**, 10587–10597.

32. N. Rybin, I. Chepkasov, D. Y. Novoselov, V. I. Anisimov, A. R. Oganov, *J. Phys. Chem. C*, 2022, **126**, 15057–15063.

33. P. P. Fedorov, V. V. Semashko, S. L. Korableva, *Inorg. Mater.* 2022, **58**, 235–

View Article Online
DOI: 10.1039/D6TC00645K

257.

34. N. I. Sorokin, D. N. Karimov, *Phys. Solid State*, 2021, **63**, 1821–1832.

35. J. W. De Wit, T. P. van Swieten, M. A. van de Haar, A. Meijerink, F. T. Rabouw, *Adv. Opt. Mater.* 2023, **2202974**, 1–7.

36. Y. Zhang, W. Ying, J. He, X. Fan, S. Xu, J. Gu, S. Liu, *Dalt. Trans.* 2023, **52**, 2948–2955.

37. C. Cressoni, F. Vurro, E. Milan, M. Muccilli, F. Mazzer, M. Gerosa, A. Speghini, *ACS Appl. Mater. Interfaces* **15**, 2023, 12171–12188.

38. J. L. B. Martin, P. S. Solanki, S. Balabhadra, Y. Alizadeh, M .F. Reid, J. P. Wells, *J. Lumin.* **233**, 2021, 117923.

39. K. de Oliveira Lima, L. F. dos Santos, M. T. de Melo, A. C. Tedesco, R. R. Gonçalves, P. Gredin, M. Mortier, *Mater. Today Commun.* **28**, 2021, 102553.

40. P. S. Solanki, S. Balabhadra, M. F. Reid, V. B. Golovko, J. R. Wells, *ACS Appl. Nanomater.* **4**, 2021, 5696–5706.

41. P. Serna-Gallén, *Crystals*, 2024, **14**, 762

42. A. P. Ayala, M. A. S. Oliveira, J-Y. Gesland and R. L. Moreira. J. Phys.: Condens. Matter 1998, **10**, 5161.

43. P. Villars and K. Cenzual, Eds., "KY3F10 Crystal Structure: Datasheet from 'PAULING FILE Multinaries Edition – 2012' in SpringerMaterials (https://materials.springer.com/isp/crystallographic/docs/sd_0552093).

44. D. J. M. Bevan, S. E. Lawton, *Acta Crystallogr. Sect. B,* 1986, **42**, 55–58.

45. P. Serna-Gallén, H. Beltrán-Mir, E. Cordoncillo, *Opt. Laser Technol.* 2021, **136**,

View Article Online
DOI: 10.1039/D6TC00645K

106734.

46. P. Serna-Gallén, H. Beltrán-Mir, E. Cordoncillo, *J. Alloys Compd.* 2021, **883**, 160847.

47. P. Serna-Gallén, H. Beltrán-Mir, E. Cordoncillo, *J. Mater. Res. Technol.* 2021, **15**, 6940–6946.

48. M. Runowski, N. Stopikowska, S. Goderski, S. Lis, *J. Alloys Compd.* 2018, **762**, 621–630.

49. M. Xin, *Opt. Laser Technol.* 2024, **170**, 110271.

50. K. S. Prichisly, *Crystals*, 2025, **15**, 500.

51. P. Serna-Gallén, H. Beltrán-Mir, E. Cordoncillo, *Ultrason. Sonochem.* 2022, **87**, 106059.

52. A. J. Garza, G. E. Scuseria, *J. Phys. Chem. Lett.* 2016, **7**, 4165–4170.

53. J. P. Perdew, W. Yang, K. Burke, Z. Yang, E. K. Gross, M. Scheffler, A. Görling, *Proc. Natl. Acad. Sci.* 2017, **114**, 2801–2806.

54. P. Serna-Gallén, H. Beltrán-Mir, E. Cordoncillo, *CrystEngComm,* 2023, **25**, 5918–5931.

55. R. D. Shannon, *Acta Crystallogr.* 1976, **A32**, 751–767.

56. A. Jain, S. P. Ong, G. Hautier, W. Chen, W. D. Richards, S. Dacek, K. A. Persson, *APL Mater.* 2013, **1**, 11002.

57. D. W. Oxtoby, H. P. Gillis, A. Campion, ed. *Cengage Learn. Belmont, CA,* 2016, (8th ed.).

58. J. D. Lee, *Concise inorganic chemistry*. John Wiley & Sons, 2008.

59. N. G. Macedo, A. F. Gouveia, R. A. Roca, M. Assis, L. Gracia, J. Andres, E. Longo, *J. Phys. Chem. C,* 2018, **122**, 8667–8679.

60. F. A. Kröger, H. I. Vink, *Solid State Phys.* 1956, **3**, 307–435.

61. M. M. Ferrer, A. F. Gouveia, L. Gracia, E. Longo, J. Andrés, *Model. Simul. Mater. Sci. Eng.* 2016, **24**, 025007.

View Article Online
DOI: 10.1039/D6TC00645K

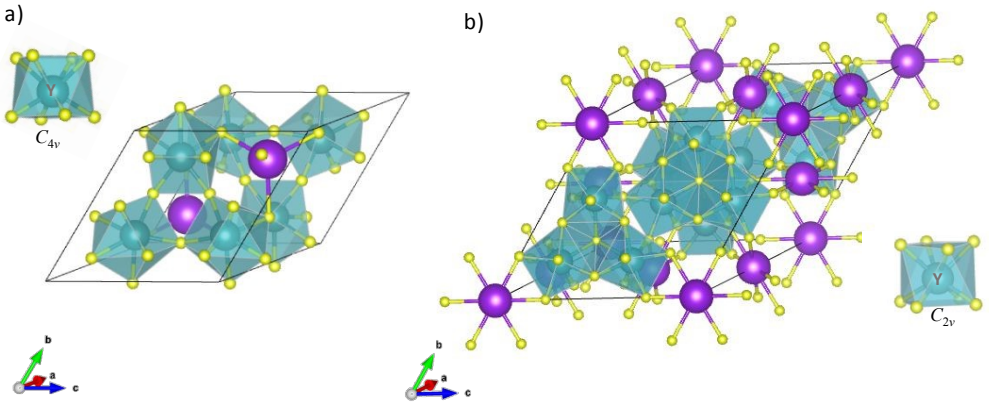

Figure 1. 3D illustration of α-KY_3F_{10} (a) and δ-KY_3F_{10} (b) structures. The local coordination of Y^{3+} cation, [YF_8] cluster, with C_{4v} and C_{2v} symmetry, respectively, is highlighted. The purple, blue and yellow spheres represent the K^+ and Y^{3+} cations, and F^-anion**.** Respectively.

View Article Online
DOI: 10.1039/D6TC00645K

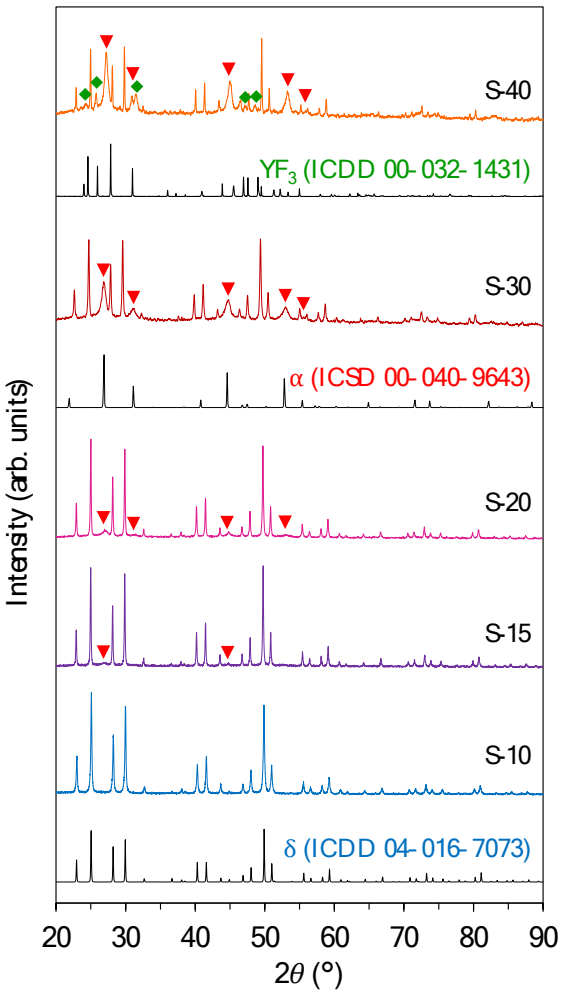

Figure 2. XRD patterns of samples doped with Eu^{3+} (S10, S15, S20, S30 and S40). XRD patterns of α– and δ–KY_3F_{10} polymorphs and YF_3 are included for comparison purposes. The peaks indicated with red triangles are associated to α-polymorph, while those highlighted with green diamonds refer to the presence of YF_3.

View Article Online
DOI: 10.1039/D6TC00645K

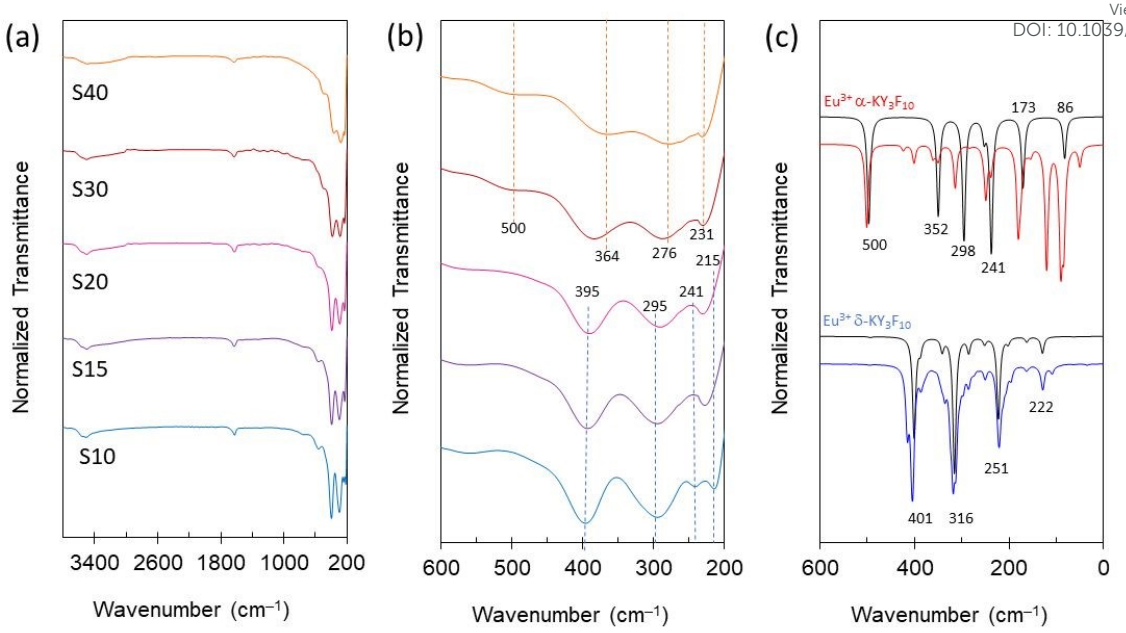

Figure 3. Experimental IR spectra of samples (a), amplified region of the spectra in the range 200-600 cm^{-1} (b), and calculated IR spectra for the α and δ crystal phases, pure (black) and doped (colored) (c). The dashed lines in (b) serve as guidelines to observe the change in the position and presence of some peaks of interest.

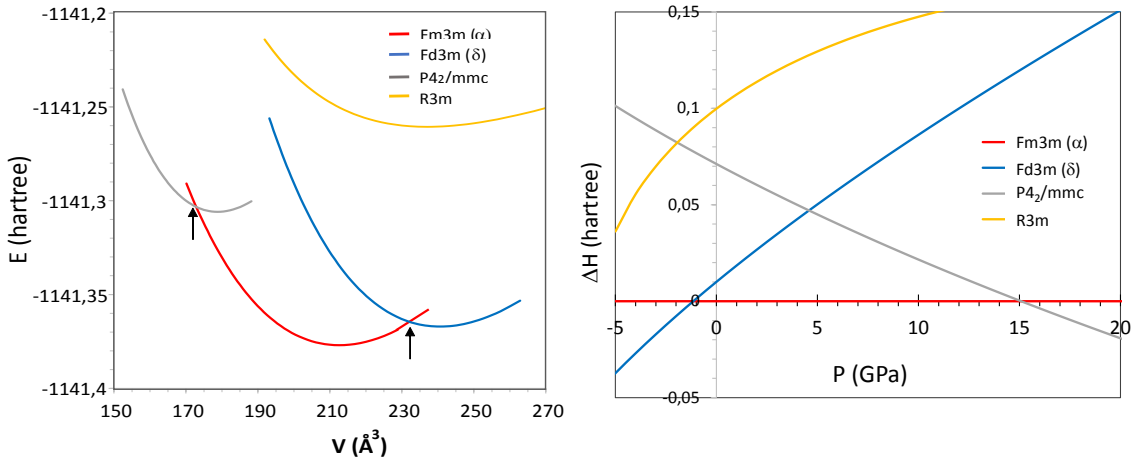

Figure 4. Energy-volume curves for the different studied polymorphs (a). Enthalpy variation of studied polymorphs as a function of pressure (b).

View Article Online
DOI: 10.1039/D6TC00645K

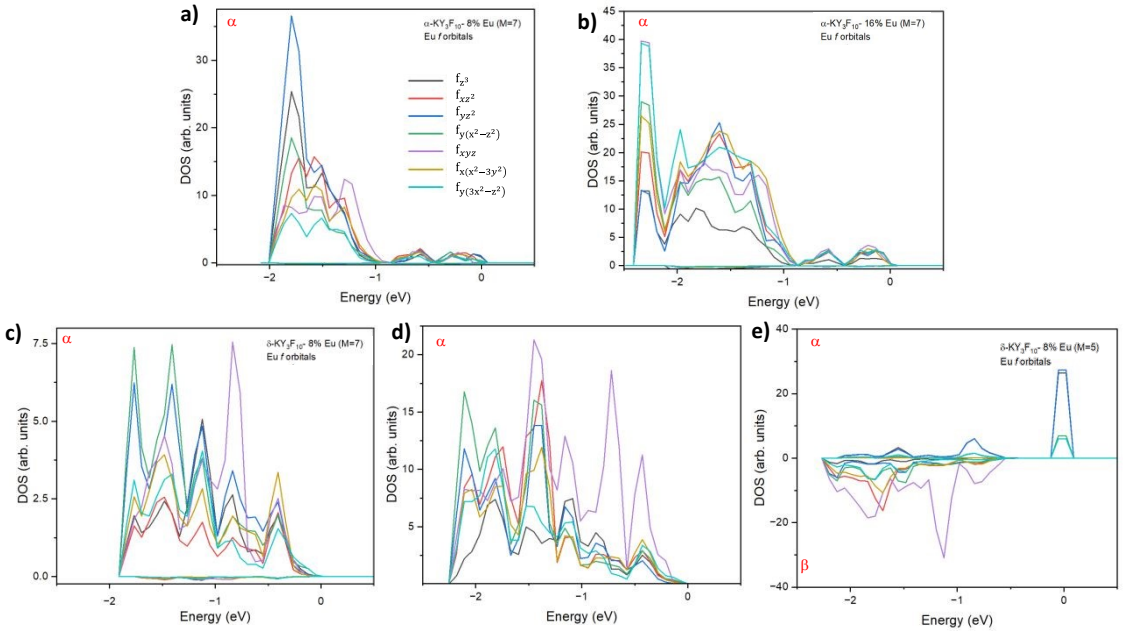

Figure 5. Projected DOS on Eu^{3+} 4f orbitals in the VB region of a) 8% Eu^{3+} (M=7) and b) 16% Eu^{3+}(M=7) for α-KY_3F_{10} polymorph, c) 8% Eu^{3+} (M=7), d) 16% Eu^{3+} (M=7) and e) 8% Eu^{3+} (M=5) for δ–KY_3F_{10} polymorph.

View Article Online
DOI: 10.1039/D6TC00645K

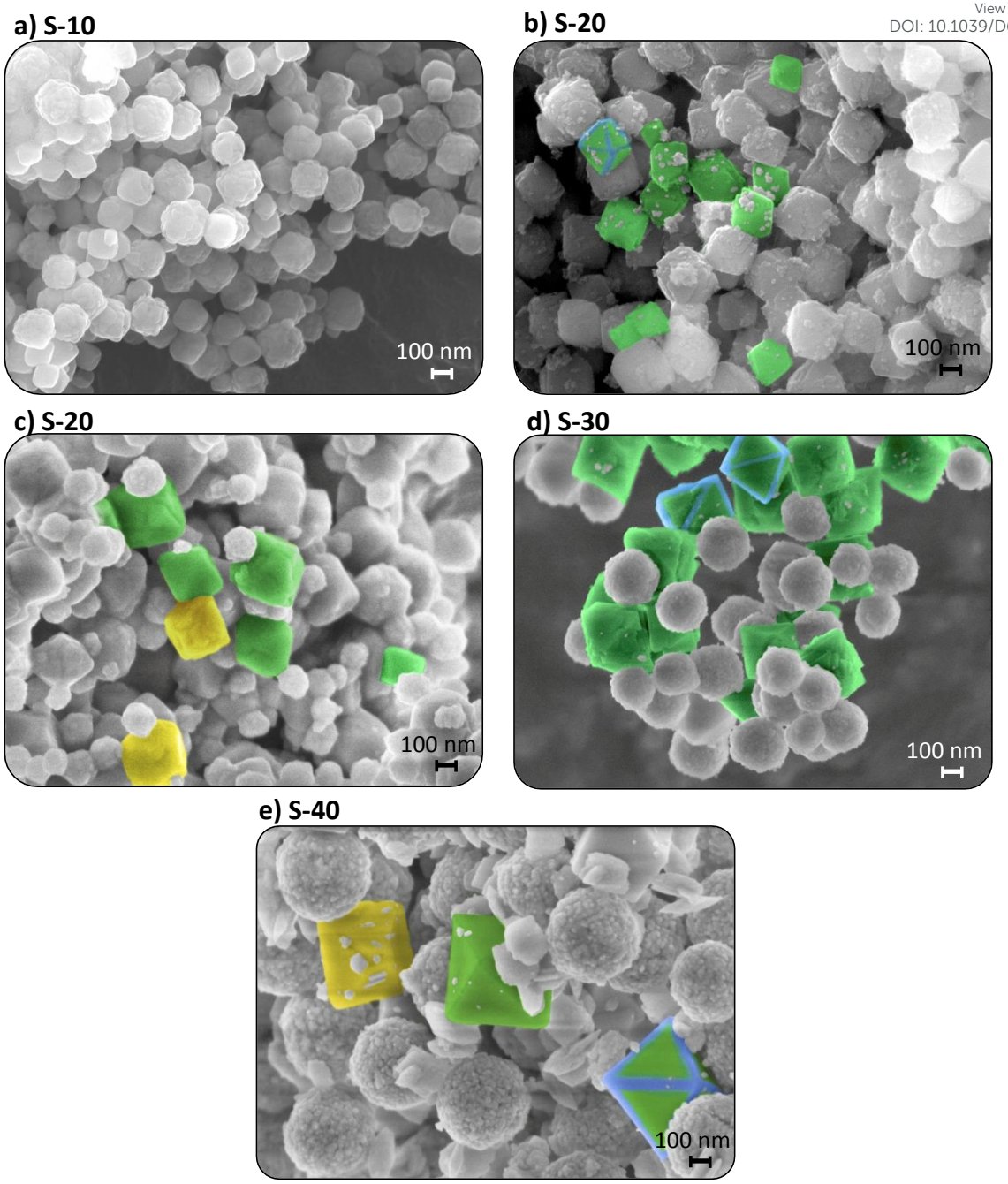

Figure 6. HRSEM images of (a) S-10, (b) S-15, (c) S-20, (d) S-30, and (e) S-40 samples. Well-defined morphologies have been pointed out in each image, and the corresponding models of octahedron, truncated octahedron, and a cube are highlighted for comparison purposes.

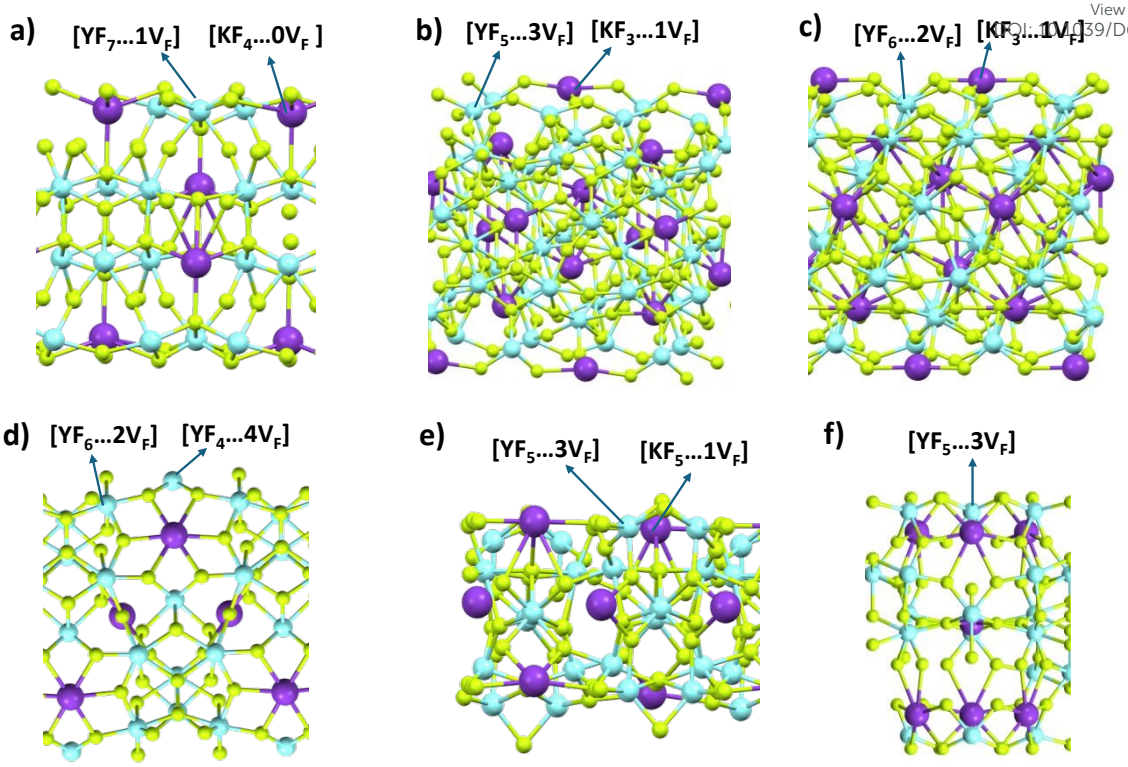

Figure 7. Surface models of the α-KY_3F_{10}, a) (100), b) (110), c) (111), and the δ-KY_3F_{10}, d) (100), e) (110), f) (111). The Y and K superficial and undercoordinated clusters on the surfaces are shown.

View Article Online
DOI: 10.1039/D6TC00645K

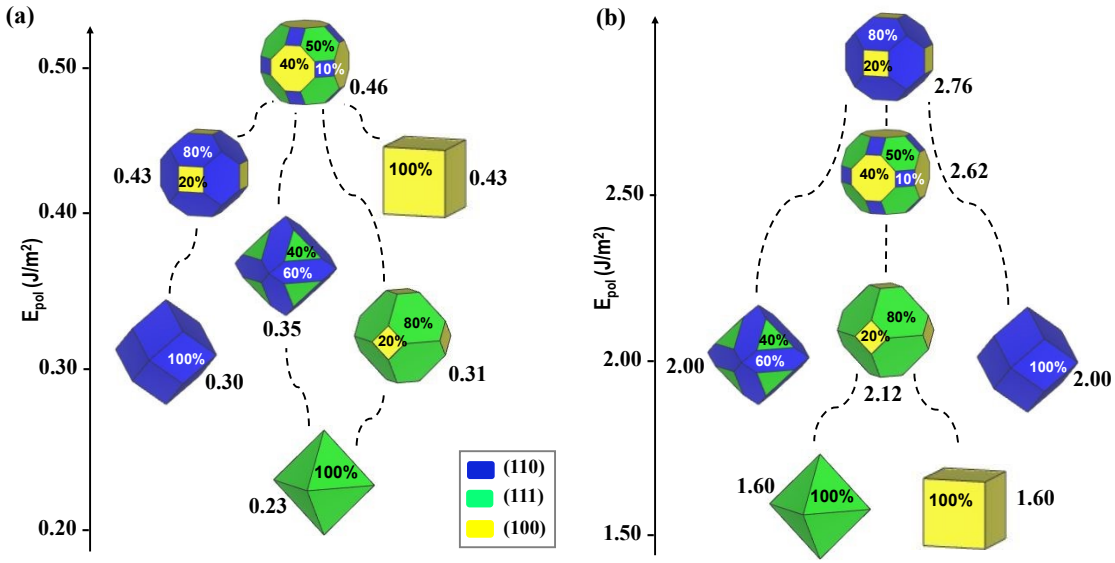

Figure 8. Map of available morphologies for (a) α-KY_3F_{10} and (b) δ-KY_3F_{10} polymorphs ordered by means of E_{pol} values.

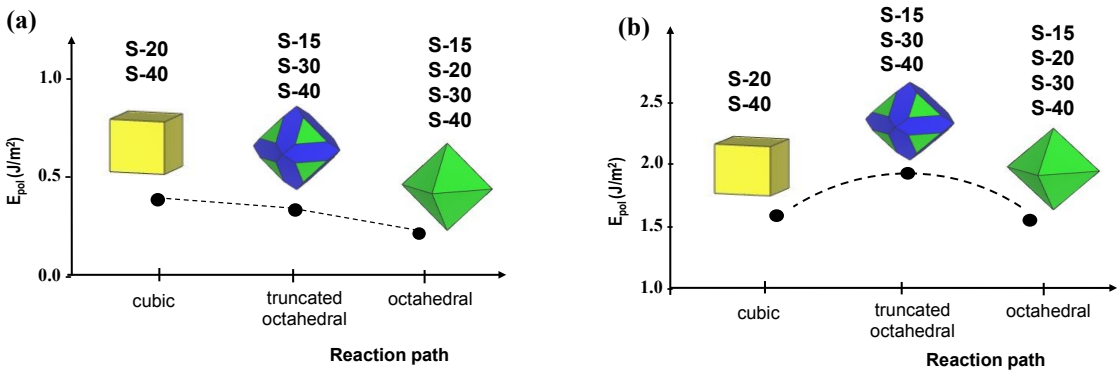

Figure 9. Polyhedron energy (E_{pol}) profiles connecting the morphologies obtained by HRSEM images and DFT calculations of (a) α-KY_3F_{10} and (b) δ- KY_3F_{10}.

View Article Online
DOI: 10.1039/D6TC00645K

Table 1. Experimental and calculated values of the geometry (cell parameters, bond lengths, and bond angles), band gap and total energy of α– and δ–KY_3F_{10} polymorphs.

		Experimental [59]	Calculated
α-KY_3F_{10}			
Cell parameter (Å)	***a***	11.52	11.66
Cell volume (Å^3)	***V***	1530.06	1587.41
Bond length (Å)	**Y-F_1 (4)**	2.19	2.21
	Y-F_2 (4)	2.34	2.36
Band gap (eV)			11.02
Total energy/f.u (eV)			-31044.275
δ-KY_3F_{10}			
Cell parameter (Å)	***a***	15.48	15.56
Cell volume (Å^3)	***V***	3711.70	3764.51
Bond length (Å)	**Y-F_1 (4)**	2.21	2.24
	Y-F_2 (2)	2.29	2.31
	Y-F_3 (2)	2.39	2.36
Band gap (eV)			11.22
Total energy/f.u (eV))			-31043.969

View Article Online
DOI: 10.1039/D6TC00645K

Table 2. Calculated values of the (cell parameters and bond lengths), band gap, and total energy of α- and δ-KY_3F_{10} polymorphs at 8.3% of Eu^{3+} doping at spin multiplicity M=7, and M=5 and 7, respectively.

			8.3% Eu doped
α-KY_3F_{10}			**M=7**
Cell volume (Å^3)	***V***		1595.78
Bond length (Å)	**Eu-F_1** **Eu-F_2**		2.26 (2) 2.27 (2) 2.37(1) 2.39(1) 2.40(2)
Band gap (eV)			4.24/8.94
Total energy/f.u (eV)			-35617.900
δ-KY_3F_{10}		**M=5**	**M=7**
Cell volume (Å^3)	***V***	3783.56	3782.98
Bond length (Å)	**Eu-F_1 (4)** **Eu-F_2 (2)** **Eu-F_3 (2)**	2.28 2.36 2.38	2.28 2.35 2.39
Band gap (eV)	**α / β**	7.48/4.85	4.94/9.03
Total energy/f.u (eV)		-35616.868	-35617.595

View Article Online
DOI: 10.1039/D6TC00645K

Table 3. Calculated values of the geometry (cell parameters and bond lengths), band gap, and total energy of α- and δ-KY_3F_{10} polymorphs at 16.7% of Eu^{3+} doping at spin multiplicity M=7.

		16.7% Eu doped
α-KY_3F_{10} supercell		**M=7**
Cell volume (Å^3)	***V***	1604,14
Bond length (Å)	**Eu-F_1** **Eu-F_2**	2.26 (2) 2.27 (2) 2.39 (3) 2.40 (1)
Band gap (eV)	**α / β**	5.5/6.65
Total energy/f.u (eV)		-40191.389
δ-KY_3F_{10}		**M=7**
Cell volume (Å^3)	***V***	3802.73
Bond length (Å)	**Eu-F_1 (4)** **Eu-F_2 (2)** **Eu-F_3 (2)**	2.29 2.35 2.39
Band gap (eV)	**α / β**	4.80/9.04
Total energy/f.u (eV)		-40191.198

View Article Online
DOI: 10.1039/D6TC00645K

Table 4. Data of thickness, area, undercoordinated clusters, E_{surf} and D_B values for studied surfaces of α and δ polymorphs.

Surface	Thickness (Å)	Area (Å^2)	E_{surf} (J/m^2)	Uncoordinated clusters	D_B (nm^{-2})
α-KY_3F_{10}					
(111)	13.33	114.59	0.92	2[YF_6…2V_F] 2[KF_3…1V_F]	5.23
(110)	12.97	114.59	1.15	2[YF_5…3V_F] 2[KF_3…1V_F]	6.98
(100)	12.08	59.85	0.43	2[YF_7…1V_F]	3.34
δ-KY_3F_{10}					
(111)	12.89	104.79	4.40	3[YF_5…3V_F]	8.59
(110)	10.42	173.73	2.80	2[YF_5…3V_F] 2[KF_5…1V_F]	4.60
(100)	14.20	121.00	2.60	2[YF_6…2V_F] 1[YF_4…4V_F]	6.61

The data supporting this article have been included as part of the Supplementary Information.

View Article Online
DOI: 10.1039/D6TC00645K